Title
Two-dimensional electronic vibrational spectroscopy and ultrafast excitonic and vibronic photosynthetic energy transfer

Journal
Faraday Discussions, 216(0)

ISSN
1359-6640

Authors
Wu, Eric C
Arsenault, Eric A
Bhattacharyya, Pallavi
et al.

Publication Date
2019-07-11

DOI
10.1039/c8fd00190a

Peer reviewed

Two-Dimensional Electronic Vibrational Spectroscopy and Ultrafast Excitonic and Vibronic Photosynthetic Energy Transfer

Eric C. Wu,[1,2] Eric A. Arsenault, [1] Pallavi Bhattacharyya,[1,2,4] Nicholas H. C. Lewis[3] and Graham R. Fleming[1,2,4]*

[1] Department of Chemistry, University of California, Berkeley 94720, USA.

[2] Molecular Biophysics and Integrated Bioimaging Division, Lawrence Berkeley National Lab, Berkeley, California 94720, USA.

[3] James Franck Institute, University of Chicago, Illinois 60637, USA.

[4] Kavli Energy Nanosciences Institute at Berkeley, Berkeley, California 94720, USA.

* Email: grfleming@lbl.gov

Abstract

Two-dimensional electronic-vibrational (2DEV) spectroscopy is a new coherent spectroscopic technique which shows considerable promise for unraveling complex molecular dynamics. In this Discussion we describe an application to the energy transfer pathway in the major light harvesting protein, LHCII, providing new data on the center line slopes (CLS) of the spectral peaks. The CLS provides information that appears unique to the 2DEV method. We then outline a general approach to calculating 2DEV spectra which is valid for strongly and weakly coupled molecular systems. We conclude with some prospects for the future development of 2DEV spectroscopy and its theoretical analysis.

Introduction

The timescale of individual energy transfer steps in the light harvesting antennas of plants, algae, and photosynthetic bacteria has been the subject of speculation and a spur to experimentalists and theorists alike for over 70 years. Once it was realized

that antenna chlorophylls (Chls) outnumbered the primary charge separation centers of Photosystem II by about 300:1, and that the quantum efficiency of transfer from the antenna at low light levels could approach 95%, it was apparent that individual energy transfer steps must be very fast given the known fluorescence lifetime of Chl. In 1964 Duysens suggested that individual steps might take 100 fs[1] while Robinson talked of exciton "spreading" as rapidly as 50 fs.[2] Such timescales were far beyond the experimental methods available in the 1960s but once mode locked lasers with few ps duration pulses became available attention rapidly turned to photosynthetic energy transport. Early measurements with low repetition rate (10^{-2} Hz!) lasers were severely compromised by the very high intensities used. With the advent of high repetition rate dye and Ti:Sapphire lasers precise measurements began to be possible notably by Gillbro, Sundstrom, and van Grondelle,[3] by Holzwarth and coworkers,[4] and by Fleming and coworkers.[5] By 1989 Eads et al. were able to roughly measure the Chl *b* to Chl *a* transfer timescale in the plant LHCII complex using fluorescence upconversion.[6] Although there were earlier hints that Forster theory based on molecule to molecule hopping was not adequate, it was the measurements of B800 to B850 transfer in the bacterial light harvesting complex 2 (LH2) protein that provided the stimulus to develop new models. It proved impossible to provide B800 to B850 transfer by simple Forster theory and simultaneously and independently, Sumi[7] and Scholes and Fleming[8] developed Generalized Forster Theory that takes account of delocalized multi-chromophore states.

Photon echo spectroscopies began to be used in the 1990s to study photosynthetic energy transfer and theoretical methods based on a modified form of Redfield theory were developed.[9–11] In 2005 Brixner et al. showed two-dimensional electronic spectra (2DES) of the bacterial FMO light harvesting complex.[12] There were hints of oscillatory behavior in the initial data but it was the 2007 paper by Engel et al. that clearly showed long-lived oscillations or beats.[13] This was followed by observations of long-lived oscillations in an alga by Scholes and coworkers[14] and temperature dependent 2DES studies of FMO by Engel and coworkers.[15] Engel et al. initially interpreted the oscillations as arising from electronic coherences between excitonic states.[13] This led to a huge surge in theoretical interest and continuing discussion of the oscillatory features as being electronic, vibronic, or vibrational in origin. Two important contributions were the development of the

Hierarchy Equations of Motion approach for formally exact calculation of energy transfer,[16] and the insightful contribution of Jonas and coworkers who showed that the longest lived oscillations were very likely from vibrational wavepackets on the ground electronic state.[17] Debate continues on the relative importance of vibronic contributions to the overall rate of transfer, compared to that from purely electronic interactions. A salutary point was made by Fujihashi et al. who showed that while oscillatory signals may be prominent in 2DES, they may have little impact on the rates of population transfer.[18]

Considering which experimental approach might be most suited to unravelling the role of vibrations in ultrafast energy transfer led us to develop a new form of 2D spectroscopy – two-dimensional electronic-vibrational (2DEV) spectroscopy.[19] In 2DEV spectroscopy two UV-vis pulses interact with the system of interest, followed by an IR pulse and finally the signal IR pulse is emitted by the system. Figure 1 shows a schematic of the relationship of 2D infrared, 2D electronic and 2DEV spectroscopies.

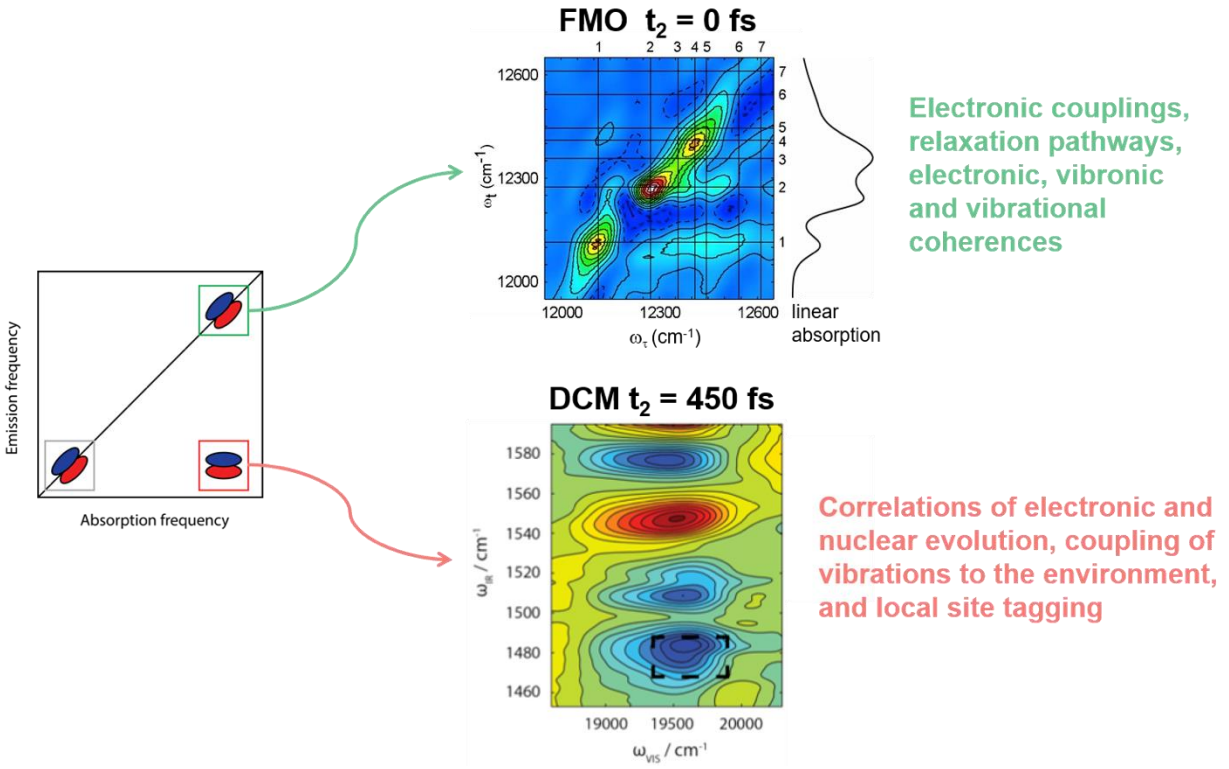

Figure 1. Two-dimensional coherent spectroscopies. Left: The positions of 2D infrared spectroscopy (lower left), 2D electronic spectroscopy (upper right), and 2D electronic-vibration (2DEV) spectroscopy (lower right) in a two-dimensional frequency plot. Right upper: The 2D electronic spectrum of the FMO light harvesting complex at waiting time (t_2T) of zero.[12] The diagonal peaks show the exciton absorption bands, the off-diagonal (cross) peaks show coupling and, at later waiting times, relaxation pathways. Right lower: 2DEV spectrum of DCM dye at t_2=450 fs.[21] There are no diagonal peaks. Excited state (absorptive) peaks are colored blue and ground state bleaches red. The box around the lower excited state peak is centered on the position of that peak at t_2=0 fs, and shows shifts in both spectral dimensions by t_2=450 fs.

2DEV spectroscopy correlates the evolution of the electronic and nuclear degrees of freedom, and thus holds promise to provide insight into the complex question of the dynamics of mixed electronic-vibrational states in natural photosynthetic light harvesting. For systems with small to moderate electronic coupling 2DEV spectroscopy also provides a window into the spatial location of excitation, since Chl vibration frequencies are sensitive to binding site, but very little dependent on whether the Chl is electronically excited or not.[20] In addition to the peak frequencies and amplitudes, the evolution of the peak shape in a 2DEV spectrum provides a novel picture of the dynamics.[21] We characterize the peak shape by a

single variable, the center line slope (CLS). In this paper we describe 2DEV spectroscopic results for the major light harvesting protein of green plants, LHCII. We then describe a new theoretical description of 2DEV spectra applicable to both weakly and strongly coupled vibronic systems. When the electronic and vibrational states become mixed, creating vibronic energy levels, the number of pathways contributing to the 2DEV signal increases substantially. By separating the response into decoherence and population relaxation contributions we show how to select the significant pathways contributing to the signal and simplify the analysis of the 2DEV spectrum.

LHCII 2DEV spectra and SVD analysis

The major pigment-protein complex utilized by plants and green algae to collect sunlight is called LHCII. About half the chlorophyll (Chl) on earth is found in this protein and the antenna systems of plants consist largely of arrays of LHCII surrounding Photosystem II supercomplexes where water splitting occurs. LHCII is generally found in trimeric form with each monomer containing 8 Chl *a* and 6 Chl *b.* Figure 2 (top panels) shows the 2DEV spectrum of LHCII at 77 K as a function of waiting time, t_2.

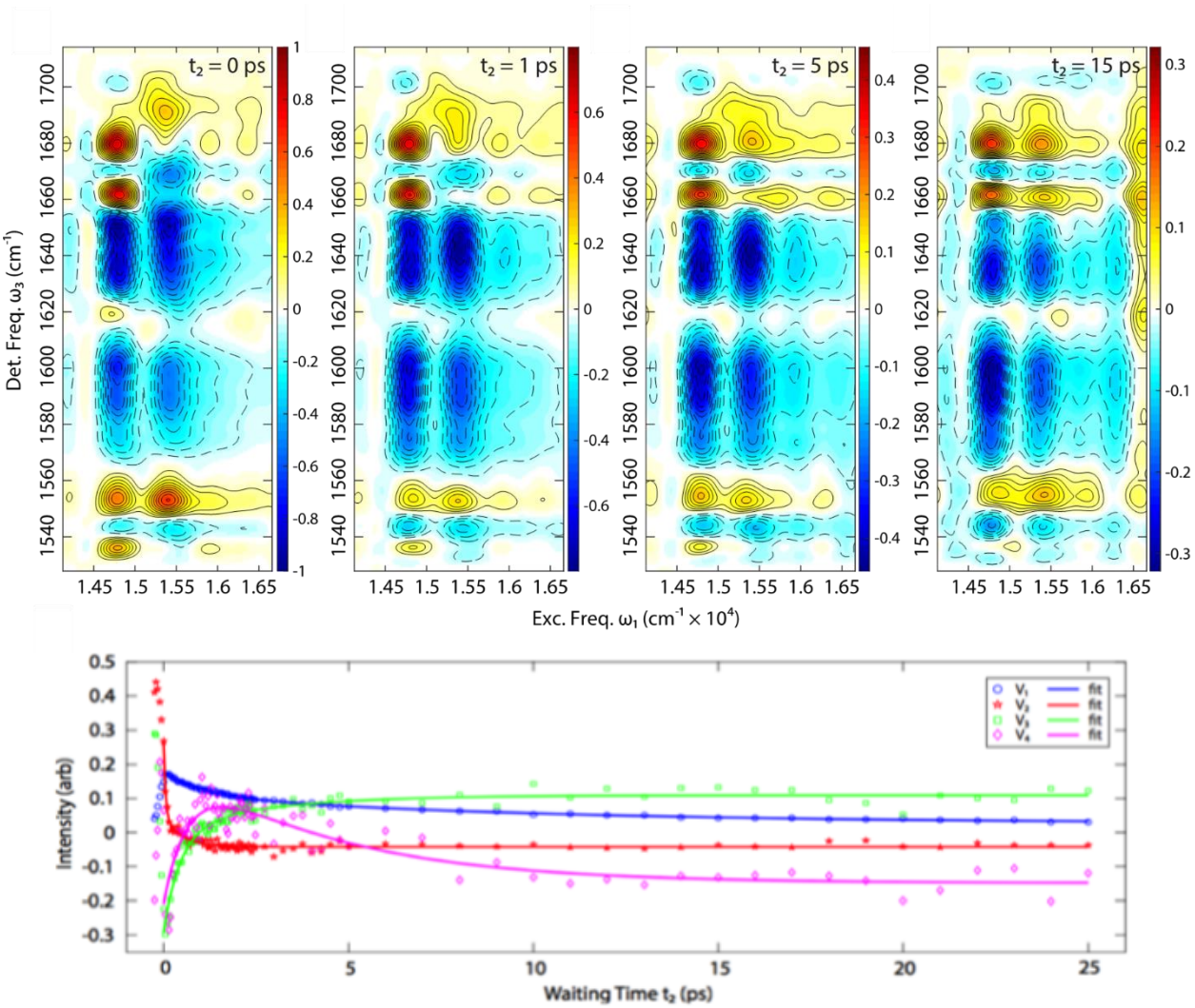

Figure 2. 2DEV spectra of the LHCII light harvesting complex at four waiting times (upper panels)[23] and singular value decomposition (SVD) into four components (lower panel). The results of fits to the four singular vectors are given in Table I. Adapted with permission from *J. Phys. Chem. Lett.*, **7**, 4197–4206. Copyright 2016 American Chemical Society.

The features in the 2DEV spectra of isolated Chl *a* and Chl *b*[22] and that of LHCII[23] have been assigned and discussed in previous works, but for clarity we will briefly summarize the main conclusions here. These assignments are based on the assumption that the vibrations remain local to either monomers or strongly coupled dimers or trimers of Chl. First, we will focus on the excitation bands, which are straightforward to assign since the transitions also appear in the linear electronic absorption spectrum of LHCII. The 14800 cm^{-1} absorption band has been assigned to electronic states associated with the Q_y transition of Chl *a*.[24,25]

However, as will be discussed below, the long-lived shoulder at 1690 cm^{-1} suggests that some long-lived population on Chl *b* contributes to this band as well. The excitation band at 15300 cm^{-1} has been assigned to a combination of Chl *b* transitions with additional contributions from higher energy Chl *a* states, such as the Q_x transition.[24,25] The shoulder above 16000 cm^{-1} is likely due to the Chl *b* Q_x transition and possibly higher energy vibronic excitations. To assign peaks along the detection axis, assignments from previous work on Chl *a* and Chl *b* were used as references.[22] The bleach at 1690 cm^{-1} in the 15400 cm^{-1} band was attributed to the five-coordinated, rather than six-coordinated, Chl *b* species as seen in the spectrum of isolated Chl *b* in solution. The 1690 cm^{-1} bleach is also present in the 14800 cm^{-1} band, but it appears slightly obscured as a shoulder of the 1680 cm^{-1} peak. The 1660 cm^{-1} and 1680 cm^{-1} bleaches present in the 14800 cm^{-1} band are likely from the same transition, possibly the GSB of C=O stretch of Chl *a*, because their intensities have the same dynamics. However, the appearance of two bleaches, rather than one, was attributed to overlap with an absorption at 1670 cm^{-1}. A peak at 1670 cm^{-1} is also present in the 15400 cm^{-1} band. The origin of the 1670 cm^{-1} transition remains unknown, as it does not appear in the spectra of isolated Chl *a* or Chl *b*. The bleaches and absorptions at 1555 cm^{-1} and 1545 cm^{-1}, respectively, were assigned to C=C stretches of the Chlorin rings. It should be noted that these peaks appear blueshifted relative to the C=C stretches observed in the spectra of isolated Chl *a* and Chl *b* due to pigment-protein interactions. The most pronounced features along the detection axis are the two broad absorptions centered at 1640 cm^{-1} and 1590 cm^{-1}. These broad absorptions were assigned to excited state absorptions (ESAs) of C=O stretches, where overlap with another feature, a ground state bleach in this case, results in the observation of two absorption features. The broadness of the C=O ESA is due to the different protein environments for the individual sites, therefore, the different dynamics between the two bands can provide information on population transfer between these sites in LHCII.

With spectral assignments as a starting point, we can now focus on the peak dynamics. The spectrum at a waiting time, t_2, of zero represents the distribution of population initially created by the laser excitation, i.e. the probe spectrum at a specific excitation frequency is given by the vibrational spectrum of the sites that are initially populated by the visible excitation at that excitation frequency.

Therefore, the differences along the detection axis between the band at 15300 cm^{-1} and 14800 cm^{-1} represent the differences between the sites that were excited. As waiting time increases, the two excitation bands become more similar due to the relaxation of the excited state population. A comparison of the spectral evolution along the detection axis of the two excitation bands then reflects both the mutual and distinct population relaxation pathways of the initial population created by the visible pump pulse. At the longest waiting time, t_2 = 15 ps, the probe spectrum along each excitation band should then be similar to the vibrational spectrum of the lowest energy state. At 77 K, this means that the equilibrated population resides in the trimer states composed of a610, a611, and a612 (the Chl numbering system is taken from Liu et al.[26]). Upon comparison of the two excitation bands, in combination with the previously discussed spectral assignments, some indication of population and energy transfer between the sites in LHCII can be observed. For example, the 15400 cm^{-1} band unambiguously shows the transfer of population from Chl *b* to Chl *a*. This is because the intensity of the 1690 cm^{-1} bleach, which as a reminder, has been assigned to Chl *b*, decreases while the intensities at the 1660 cm^{-1} and 1680 cm^{-1} bleaches, both assigned to Chl *a*, increase. Inspection of the two broad C=O ESAs also reveals population transfer, in this case from the 1640 cm^{-1} peak, assigned Chl *b*, to the 1590 cm^{-1} peak of Chl *a*.

To further study the dynamics, singular value decomposition (SVD) was performed on the spectrum. SVD breaks the spectrum into different spectral surfaces and dynamical contributions weighted by the singular values. SVD analysis gives the corresponding four spectral components that are not dominated by noise, shown in Figure 3. The first four singular vectors are shown in the lower panel of Figure 2. Table I collects the results of biexponential fits to these curves.

Table I. Biexpontial fits to the four singular vectors in Figure 2

Fit to $V_i(t) = A_1 e^{-t/\tau_1} + A_2 e^{-t/\tau_2} + A_3$

	A_1	τ_1 (ps)	A_2	τ_2 (ps)	
V_1	0.07	1.13	0.08	9.97	Overall relaxation of spectrum
V_2	0.22	0.05	0.09	0.50	b → a transfer a → a' relaxation
V_3	-0.30	0.46	-0.10	2.90	Equilibration to "bottleneck" states
V_4	-0.45	0.67	0.39	4.21	Resolved intermediates along the relaxation pathway

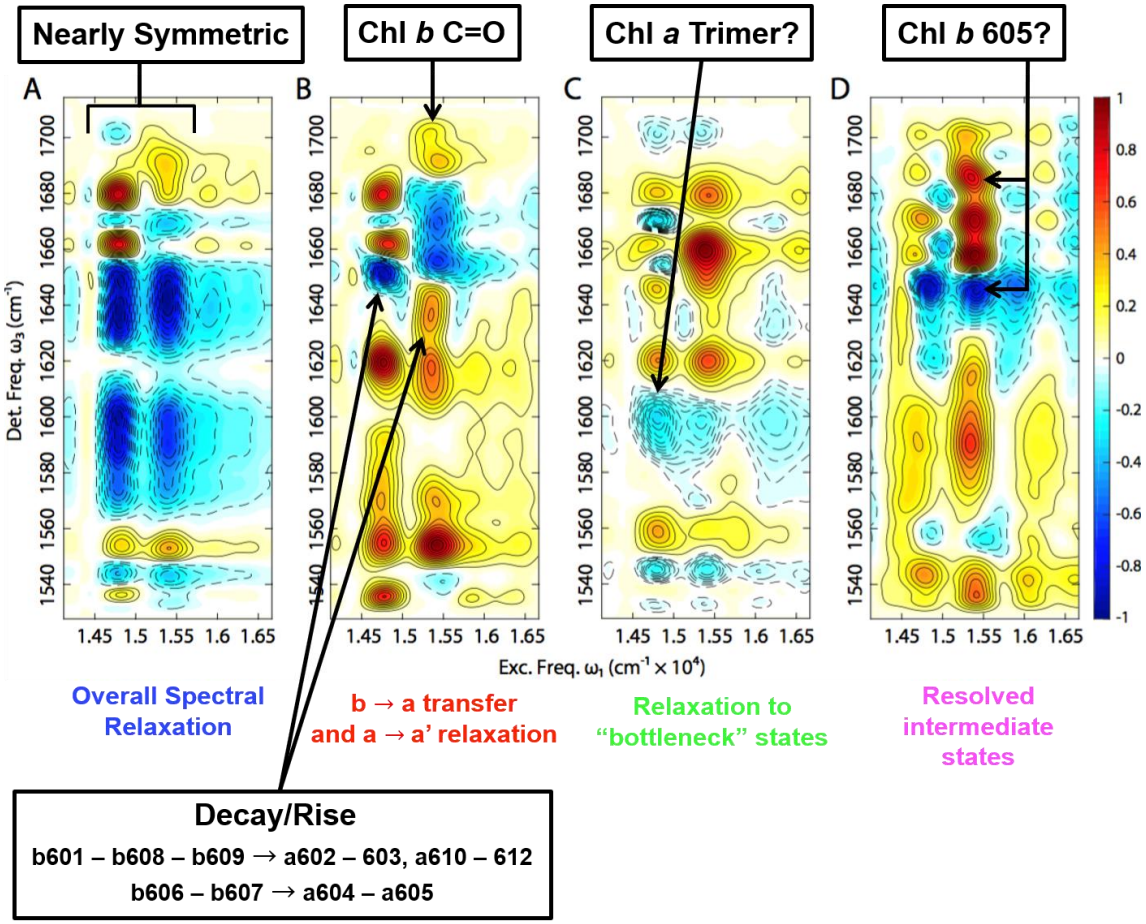

Figure 3. SVD spectral components corresponding to the four singular vectors (A-D) in Figure 2.[23] Assignments of a number of the spectral features are shown on the figure while overall relaxation pathways are indicated below. Note the nearly symmetric appearance of the first panel, indicating overall relaxation.[23] Adapted with permission from *J. Phys. Chem. Lett.*, **7**, 4197–4206. Copyright 2016 American Chemical Society.

The first component, the spectral surface and corresponding dynamical component with the largest singular value, is what best describes the 2DEV spectrum. The second component is then the surface and dynamics that best describes the 2DEV spectrum once the first component is removed. The first spectral surface is very similar to the 2DEV spectrum at waiting time of 1 ps. This indicates that the changes in the spectrum as a function of waiting time are minor and the dynamics of the first component reflect the overall decay of the spectrum as the population returns from excited state to ground state. The second spectral component, which is notably the only component beside the first to have a peak at 1690 cm^{-1}, shows the relaxation both from Chl *b* to Chl *a* and within Chl *a*. In the 15400 cm^{-1} band, the second spectral component has a positive peak at 1690 cm^{-1} and two negative peaks at 1680 and 1660 cm^{-1}. This solidifies the earlier claim of the observation of population transfer from Chl *b* to Chl *a*. Moreover, in the second spectral component, the differences in the C=O ESA region, 1570 cm^{-1} to 1650 cm^{-1}, between the two excitation bands reveal the different relaxation pathways for these bands. Starting with the 14800 cm^{-1} band, the negative peak at 1650 cm^{-1} and the positive peak at 1620 cm^{-1} indicate that the population relaxes directly from 1650 cm^{-1} to 1620 cm^{-1}. On the other hand, for the 15300 cm^{-1} band, the additional positive peak at 1640 cm^{-1} indicates a completely different or an additional relaxation pathway. The dynamics belonging to the second spectral surface, which again has been attributed to Chl *b* to Chl *a* relaxation, was best fit with an biexponential function with time constants of 50 fs and 0.5 ps. The dynamics of the third component, which rises then plateaus, suggest that the third spectral surface represents the lowest energy state, possibly the Chl *a* trimer. Finally, the fourth component, exhibiting a rise followed by a decay, suggest that the fourth spectral surface may be attributed to intermediate species. While it is clear that 2DEV spectroscopy can provide remarkable insight into the dynamics of complex systems it is also clear that further theory and modeling is needed to fully assign the abundance of observed transitions and to unveil the wealth of information contained within these experiments.

LHCII Center Line Slope data and analysis

Information that may be unique to 2DEV spectra can be obtained via analysis of the center line slope (CLS) dynamics of the spectral features. The CLS describes the correlation between initial electronic coherence created by the first visible pulse

and the final vibrational coherence created by the IR probe pulse. The CLS can be positive, negative, or zero. A non-zero center line slope indicates that there is a correlation between the initial electronic and final vibrational transitions. For LHCII, prior to calculating the CLSs, we did not expect to see any correlations, especially long-lived correlations, due to the rapid energy and population transfer in LHCII. Instead, we expected that population and energy transfer would scramble and ultimately destroy any correlation between electronic and vibrational coherences. However, contrary to intuition, CLSs with a rich variety of dynamics were observed, as can been seen in Figure 4.

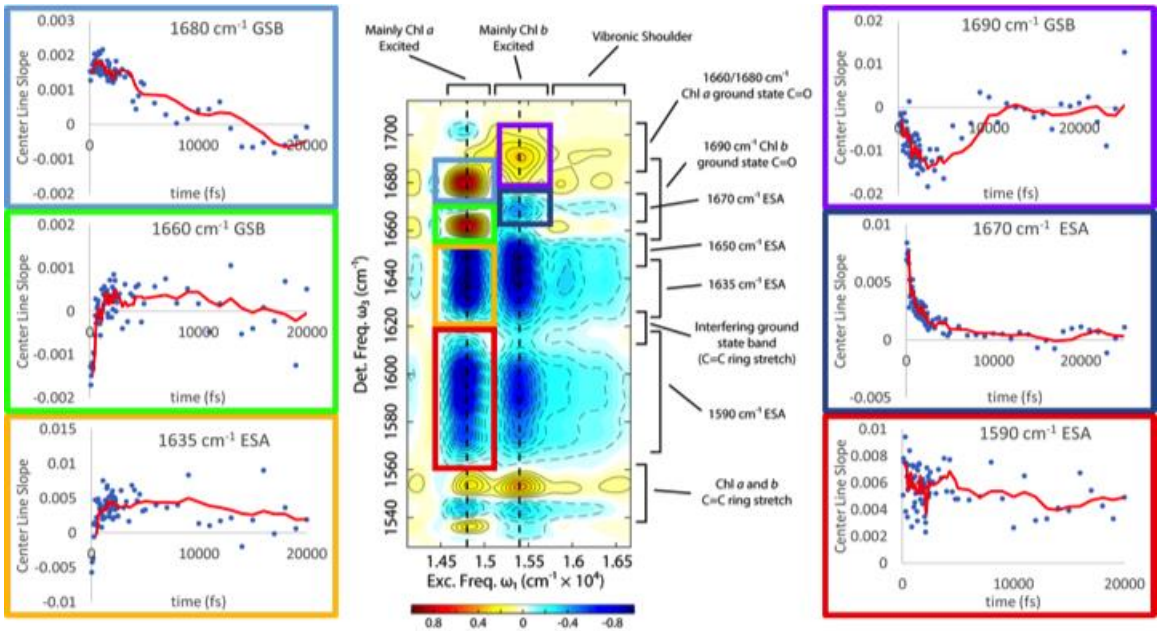

Figure 4. Center line slopes (CLS) for the peaks indicated in the central panel by colored boxes. Note the wide variation in sign and time dependence of the CLS for different spectral features.

The CLSs for some peaks were not shown for one of two reasons: either the CLS dynamics were similar to those of other peaks for which the CLS dynamics were already shown or the CLSs were zero throughout the entire waiting time. Some CLSs decay monotonically and rapidly, such as the 1670 cm^{-1} ESA, and some decay monotonically and slowly, such as the 1590 cm^{-1} ESA and the 1680 cm^{-1} GSB. The CLS of the 1670 cm^{-1} ESA decays with a time constant of 0.9 ps, therefore the decay of the CLS is likely due to the population of Chl *b* to Chl *a* destroying the correlation. The CLS of the 1590 cm^{-1} ESA of the 14800 cm^{-1} band decays very slowly and appears to plateau. Since the spectrum is measured at 77K, the long-lived

correlation may be due to a static inhomogeneous contribution, because of the frozen protein environment. On the other hand, the CLS of the 1590 cm^{-1} ESA of the 15300 cm^{-1} band is zero for all waiting times. This could indicate that the static contribution to the CLS was lost due to population transfer. In addition to CLSs that decay monotonically, some CLSs exhibit sign changes from negative to positive, such as the 1660 cm^{-1} GSB and the 1635 cm^{-1} ESA, and some decrease from zero to negative values, then decay back to zero, such as the 1690 cm^{-1} GSB. While the underlying causes of the observed CLS dynamics remain to be detailed, a previous 2DEV study on triphenylmethane dyes[27] argued that a change in the sign of CLS could indicate a change in the overall molecular dipole moment due to changes in the electronic structure. The fast initial rise in the CLSs of the 1660 cm^{-1} GSB and the 1635 cm^{-1} ESA can be fit with time constants of 0.4 ps and 0.2 ps, suggesting that the initial rise could be due to large changes in the overall dipole direction due to population relaxation from Chl *b* to Chl *a*. Moreover, it is interesting to note that even though the 1680 cm^{-1} GSB and the 1660 cm^{-1} GSB have identical dynamics in terms of peak intensities, these features exhibit quite different CLS dynamics. The distinction between the peak intensity and the CLS dynamics could simply be due to overlap with the 1670 cm^{-1} ESA, or more intriguingly, it could indicate that these two peaks are from the same exciton, but different sites. For example, the 1680 cm^{-1} and the 1660 cm^{-1} GSBs come from C=O stretches on different Chls in different environments, which result in the CLSs having different signs. Finally, some CLSs appear to have oscillations during the first ps, which could be caused by vibronic coherences, which is an area of particular interest in the development of theoretical models. However, to confirm such a claim, more waiting times must be sampled. Ultimately, the full interpretation of CLS dynamics is contingent on further theoretical development.

Theoretical Modeling of 2DEV Spectra

To theoretically evaluate nonlinear spectra, we can proceed in two different ways: a) calculate the net nonlinear polarization: nonperturbative approaches[28–30] are generally used to theoretically evaluate polarization, however, this approach offers limited insights and requires extensive post-processing[31] to extract the spectroscopic signal and, b) evaluate the Nonlinear Response Functions (NRFs),[32]

relevant to the pulse sequence: NRFs are mathematically expressed in terms of the transition dipole moments describing the field-matter interactions at the different times of the spectroscopy and offer more readily apparent physical insight, than comes from calculating the polarization. Numerical methods, for instance, the Liouville Hierarchical Equation of Motion method,[33] are employed to evaluate the NRFs. However, such numerical methods are computationally expensive and scale poorly with the system dimensionality.

To circumvent this problem, we propose a near-analytical theoretical approach to evaluate NRFs for 2DEV spectroscopy. The principal approximation we employ to achieve analyticity is that non-adiabatic transitions among the system states could be treated perturbatively, which implies that the system resides close to its adiabatic limit. The principal goal is not to obtain exact results, for which we need extensive numerical simulations but to obtain an understanding of how 2DEV spectroscopy can help to unravel the mechanism of excitation energy transfer in light-harvesting complexes, both spatially and temporally. Analyticity ensures more expedient calculations and provides clear insights. The key feature of the near-analytical approach we introduce for 2DEV spectroscopy is a unitary transformation, analogous to the one used for the non-adiabaticity theory in chemical dynamics.[34]

For our initial calculations, we consider a model dimer system, with an IR mode, of angular frequency ω $(\omega = \omega_A = \omega_B,\ \hbar = 1)$, local to each of the monomers (monomers labeled as A and B, respectively). We consider the IR modes on A and B to be uncoupled. The electronic coupling is given as $\langle A|H|B\rangle = \langle B|H|A\rangle = J$. The site basis, given as $\left|X\ v_\mu^A v_\nu^B\right\rangle$, therefore, should reflect information about both the electronic and IR modes. Here, $X\ \in \{g, A, B\}$, where g labels the electronic state where both A and B are in their respective ground states, A labels the state where only A is electronically excited and B labels the state where only B is electronically excited. We do not consider the doubly-excited electronic state, which is not important in 2DEV spectroscopy. The superscript on v in $\left|X\ v_\mu^A v_\nu^B\right\rangle$ denotes that the IR mode is local to A or B, and $\{\mu, \nu\} \in \{g0, g1, e0', e1'\}$. Here, g and e denote the ground and first excited electronic states, respectively, for the

given monomer. 0 and $0'$ are the ground vibrational states on the ground and first excited electronic states, respectively. Similarly, 1 and $1'$ are the first excited vibrational states on the ground and first excited electronic states, respectively. For simplicity, in the site basis, the electronic wavefunctions are considered to be independent of the nuclear wavefunctions, i.e., $\left|X\ v_\mu^A v_\nu^B\right\rangle \approx |X\rangle\otimes\left|v_\mu^A\right\rangle\otimes|v_\nu^B\rangle$. The vibrational overlap between the nuclear wavefunctions on the ground and excited electronic states, for a given monomer, are expressed in terms of the Huang Rhys factors σ:

$$\left\langle v_{g0}^A\middle|v_{e0'}^A\right\rangle = e^{-\frac{\sigma}{2}}; \left\langle v_{g0}^A\middle|v_{e1'}^A\right\rangle \approx -\left\langle v_{e0'}^A\middle|v_{g1}^A\right\rangle = \sqrt{\sigma}e^{-\frac{\sigma}{2}}; \left\langle v_{g1}^A\middle|v_{e1'}^A\right\rangle = (1-\sigma)e^{-\frac{\sigma}{2}} \tag{1}$$

Again, the ground and excited electronic states are coupled only radiatively. Consequently, for the Ground State Bleaching (GSB) pathway, we work with the system Hamiltonian in the ground electronic state manifold, $H_{sys,g}$, formed by the basis states, $\left|g\ v_{g0}^A v_{g0}^B\right\rangle$, $\left|g\ v_{g1}^A v_{g0}^B\right\rangle$ and $\left|g\ v_{g0}^A v_{g1}^B\right\rangle$, respectively. The ground electronic state is considered to be the zero of energy.

$$H_{sys,g} = \begin{pmatrix} 0 & 0 & 0 \\ 0 & \omega & 0 \\ 0 & 0 & \omega \end{pmatrix} \tag{2}$$

For the Excited State Absorption (ESA) pathway, we work with the system Hamiltonian in the excited electronic state manifold, $H_{sys,ex}$, formed by the basis states $\left|A\ v_{e0'}^A, v_{g0}^B\right\rangle$, $\left|A\ v_{e1'}^A, v_{g0}^B\right\rangle$, $\left|A\ v_{e0'}^A, v_{g1}^B\right\rangle$, $\left|B\ v_{g0}^A v_{e0'}^B\right\rangle$, $\left|B\ v_{g0}^A v_{e1'}^B\right\rangle$, and $\left|B\ v_{g1}^A v_{e0'}^B\right\rangle$, respectively.

$H_{sys,ex} =$

$$\begin{pmatrix} E_A & 0 & 0 & Je^{-\sigma} & J\sqrt{\sigma}e^{-\sigma} & -J\sqrt{\sigma}e^{-\sigma} \\ 0 & E_A+\omega' & 0 & J\sqrt{\sigma}e^{-\sigma} & J\sigma e^{-\sigma} & J(1-\sigma)\sqrt{\sigma}e^{-\sigma} \\ 0 & 0 & E_A+\omega & -J\sqrt{\sigma}e^{-\sigma} & J(1-\sigma)e^{-\sigma} & J\sigma e^{-\sigma} \\ Je^{-\sigma} & J\sqrt{\sigma}e^{-\sigma} & -J\sqrt{\sigma}e^{-\sigma} & E_B & 0 & 0 \\ J\sqrt{\sigma}e^{-\sigma} & J\sigma e^{-\sigma} & J(1-\sigma)e^{-\sigma} & 0 & E_B+\omega' & 0 \\ -J\sqrt{\sigma}e^{-\sigma} & J(1-\sigma)\sqrt{\sigma}e^{-\sigma} & J\sigma e^{-\sigma} & 0 & 0 & E_B+\omega \end{pmatrix}$$

(3)

Here, the displaced IR mode in the excited electronic state has a shifted frequency ω'. The first excited electronic states of A and B have energies, E_A and E_B, respectively. The system interacts with the environment/ bath/ phonons, considered to be a collection of harmonic oscillators. Therefore, the total Hamiltonian including the system, bath and the system-bath coupling, approximated to be linear in the position coordinates of the phonon harmonic oscillators, is given as:

$$H_{g/ex} = \sum_i (E_i + Q_i)|i\rangle\langle i| + \sum_{i,j,i\neq j} V_{ij}\,|i\rangle\langle j| + H_{ph},$$

(4)

where

$$H_{ph} = \sum_{i,k}\left(\frac{p_{ik}^2}{2m_{ik}} + \frac{1}{2}m_{ik}\omega_{ik}^2 q_{ik}^2\right),$$

(5)

where i runs over 3 basis states, as discussed above, for H_g and 6 basis states for H_{ex}. V_{ij} describes the off-diagonal coupling between the system states, k labels the harmonic oscillator. The system-bath coupling is defined as $Q_i = \sum_k m_{ik}\nu_{ik}q_{ik}$. q_{ik}, m_{ik}, ν_{ik}, ω_{ik} and p_{ik} are the position, mass, coupling strength, angular frequency and momentum, respectively, of the k^{th} oscillator pertaining to the i^{th} system state. H_g is diagonal with respect to its basis and therefore, easy to work with. H_{ex}, on the other hand, when diagonalized, is given as:

$$H_{ex} = \sum_m \varepsilon_m(\boldsymbol{Q})|m(\boldsymbol{Q})\rangle\langle m(\boldsymbol{Q})| + H_{ph},$$

(6)

where $|m(\boldsymbol{Q})\rangle$ denotes the adiabatic basis. The adiabatic basis is tedious due to its dependence on $\boldsymbol{Q}$, the system-bath coupling vector. Also, it does not commute with the momenta in H_{ph}. We, therefore, introduce a unitary transformation, $U(\boldsymbol{Q})$, which transforms from the adiabatic basis $|m(\boldsymbol{Q})\rangle$ to the stationary adiabatic basis $|m(\boldsymbol{Q}=\boldsymbol{0})\rangle$, to be denoted as $|m\rangle$.[35–37]

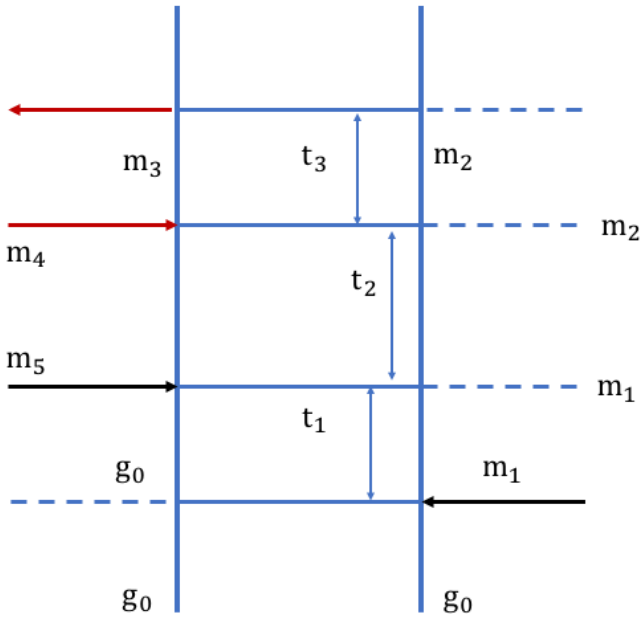

Figure 5. Feynman diagram for an excited state rephasing pathway. Electronic interactions with the light are shown as black arrows, infrared interactions as red arrows. m_i denotes a vibronic level.

The 2DEV spectra can be theoretically evaluated from the relevant response functions, using Feynman diagrams. As an example, we will discuss in detail the calculation for the ESA rephasing pathway shown in Figure 5, the other pathways are evaluated in an analogous fashion. To ease the notation, g_0 will now denote the state $\left|g\ v_{g0}^{A} v_{g0}^{B}\right\rangle$. The m_i states, where i is a positive integer, are used to denote the stationary adiabatic basis states. Despite the different definition, the stationary adiabatic basis states have same energies as the eigenstates obtained by diagonalizing the system Hamiltonian in the electronic excited state manifold, $H_{sys,ex}$. The ESA rephasing response function can be written as:

$$\mathrm{R_{ESA}}(t_3, t_2, t_1) = -\langle \mu_{el}(0)\mu_{vib}(t_1+t_2+t_3)\mu_{vib}(t_1+t_2)\mu_{el}(t_1)\rho(0)\rangle,$$

(7)

where $\rho(0) = |g_0\rangle\langle g_0|\rho_{ph}(0)$. $\mu_{el/vib}(t)$ is the transition dipole operator in the Heisenberg picture at time t, defined as $\mu_{el/vib}(t) = e^{iH_{ex}t}\,\mu_{el/vib}e^{-iH_{ex}t}$. Therefore,

$$\begin{aligned}&\mathrm{R}_{\mathrm{ESA}}(t_3,t_2,t_1)\\&= -Tr_{ph}\{\langle g_0|\mu_{el}e^{iH_{ex}\,(t_1+t_2+t_3)}\mu_{vib}e^{-iH_{ex}t_3}\,\mu_{vib}e^{-iH_{ex}t_2}\,\mu_{el}e^{-iH_{ex}t_1}\,|g_0\rangle\rho_{ph}(0)\}.\end{aligned}$$

(8)

Introducing the unitary transformation and the stationary adiabatic basis,[35–37] we have

$$\begin{aligned}&\mathrm{R}_{\mathrm{ESA}}(t_3,t_2,t_1)\\&= -\sum_{\{m\}}\mu_{el,g_0m_1}\mu_{vib,m_2m_3}\mu_{vib,m_3m_4}\mu_{el,m_5g_0}\,e^{-iH_{ph}t_1}\,\mathrm{F}_{m_1m_2m_3m_4m_5}(t_3,t_2,t_1),\end{aligned}$$

(9)

where

$$\begin{aligned}&\mathrm{F}_{m_1m_2m_3m_4m_5}(t_3,t_2,t_1)\\&\qquad= Tr_{ph}\{\langle m_1|e^{i\bar{H}_{ex}t_1}\,|m_1\rangle\langle m_1|e^{i\bar{H}_{ex}t_2}\,|m_2\rangle\langle m_2|e^{i\bar{H}_{ex}t_3}\,|m_2\rangle\\&\qquad\times\langle m_3|e^{-i\bar{H}_{ex}t_3}\,|m_3\rangle\langle m_4|e^{-i\bar{H}_{ex}t_2}\,|m_5\rangle\rho_{ph}(0)\}.\end{aligned}$$

(10)

Here, $\bar{H}_{ex} = \bar{H}_0 + \bar{H}_{na}$, where $\bar{H}_0 = \sum_m \varepsilon_m(\boldsymbol{Q})|m\rangle\langle m| + H_{ph}$ and $\bar{H}_{na}$ is the perturbative term.[35,36] We have approximated above that $\langle g_0|\mu|m_i(\boldsymbol{Q})\rangle \approx \langle g_0|\mu|m_i\rangle$. In the 2DEV experiments, t_1 and t_3 are small, so we can neglect population relaxation during these times. The dynamics time t_2 could be small or large — if it is large compared to phonon relaxation time, population relaxation needs to be accounted for. If t_2 is small, we can neglect population relaxation, therefore, $m_1 = m_2$ and $m_4 = m_5$. We now make the approximation that, since decoherence and incoherent population relaxation are largely independent processes, we can decouple them at the lowest order. Introducing $\bar{H}_0$ [35,36] and working in the interaction picture, we obtain:

$$
\begin{aligned}
&\mathrm{F}_{m_1 m_2 m_3 m_4 m_5}(t_3, t_2, t_1) \\
&\approx Tr_{ph}\left\{\left(\hat{T}^{\dagger} e^{i\int_0^{t_1} dt' \varepsilon_{m_1}\left(\boldsymbol{Q}(t')\right)}\right)\left(\hat{T}^{\dagger} e^{i\int_0^{t_2} dt' \varepsilon_{m_2}\left(\boldsymbol{Q}(t')\right)}\right)\left(\hat{T}^{\dagger} e^{i\int_0^{t_3} dt' \varepsilon_{m_2}\left(\boldsymbol{Q}(t')\right)}\right)\right. \\
&\left.\times\left(\hat{T} e^{-i\int_0^{t_3} dt' \varepsilon_{m_3}\left(\boldsymbol{Q}(t')\right)}\right)\left(\hat{T} e^{-i\int_0^{t_2} dt' \varepsilon_{m_4}\left(\boldsymbol{Q}(t')\right)}\right)\rho_{ph}(0)\right\} e^{iH_{ph}t_1} \\
&\times Tr_{ph}\left\{\left\langle m_1\middle|\mathrm{U}_I^{\dagger}(t_2)\middle|m_2\right\rangle \rho_{ph}(0)\langle m_4|\mathrm{U}_I(t_2)|m_5\rangle\right\},
\end{aligned}
\tag{11}
$$

where $\hat{T}^{\dagger} e^{i\int_0^t dt' \varepsilon_{m_i}\left(\boldsymbol{Q}(t')\right)} = e^{i\varepsilon_{m_i} t}\left(\hat{T}^{\dagger} e^{i\int_0^t dt' \nabla_{\boldsymbol{Q}} \varepsilon_{m_i}\left(\boldsymbol{Q}(t')\right).\boldsymbol{Q}(t')}\right)$, and the phonon coupling to the m_i state in $\boldsymbol{Q}$ causes decoherence, evaluated almost exactly for an Ohmic or Debye spectral density for the environment, while $\mathrm{U}_I(t) = e^{i\bar{H}_0 t}\, e^{-i\bar{H}_{ex} t}$, and $Tr_{ph}\left\{\left\langle m_1\middle|\mathrm{U}_I^{\dagger}(t_2)\middle|m_2\right\rangle \rho_{ph}(0)\langle m_4|\mathrm{U}_I(t_2)|m_5\rangle\right\}$ results in population relaxation and is treated perturbatively by a Markovian master equation.[35,36].This is justified since the system is assumed to stay close to its adiabatic limit and therefore, non-adiabatic transitions leading to population relaxation among the stationary adiabatic states are treated perturbatively.

Results and Discussion

For the ESA rephasing pathway, as seen in Fig. 5, we will have 6^5possible pathways, since m_i, where $i \in \{1,2,3,4,5\}$, could be any of the 6 states obtained by diagonalizing $H_{sys.ex}$. Since we are seeking mechanistic insights into the dynamics, it would be valuable to look at each of these individual pathways and the respective contributions. However, performing calculations for 6^5 pathways is tedious and despite the near-analyticity that the method promises, time-consuming. We exploit the separability of the transformed Hamiltonian into decoherence and population relaxation. The population relaxation rates,[35,36] which are given as,

$$
\Gamma_{mn} = 2\pi \frac{1}{e^{\beta\omega_{mn}} - 1} \sum_j J_j(\omega_{mn})(\langle n|j\rangle \langle j|m\rangle)^2,
\tag{12}
$$

and $\Gamma_{nm} = e^{\beta\omega_{mn}}\Gamma_{mn}$, where m, n label the stationary adiabatic states, j labels the site state, $J_j(\omega)$ is the spectral density for the j^{th} site and $\omega_{mn} = \varepsilon_m(\mathbf{0}) - \varepsilon_n(\mathbf{0}), \omega_{mn} > 0$, allow us to select the significant pathways; we discard those that have very small rates. Also, we can neglect pathways that have small values for the transition dipole moments. Using the two tools, we are able to significantly reduce the number of pathways we need to compute to obtain the spectroscopic signal.

In our calculations, we choose $\mu_{el} = 1$ for both the monomers A and B, in the site basis. Also, the values for the vibrational transition dipole moments μ_{vib}, in the site basis are considered to be unity. $E_A = 12000\ cm^{-1}$, $E_B = 12450\ cm^{-1}$, $J = 250\ cm^{-1}$, $\omega = 1030\ cm^{-1}$, $\omega' = 950\ cm^{-1}$, $\sigma = 0.0025$ and $T = 77\ K$. The ratio of the displacements for the IR mode in the ground and excited vibrational states in the electronic excited state with respect to the ground electronic state are given as $\alpha_0 = 0.6$ and $\alpha_1 = 1.6$, respectively.[21] The environment is modeled by the Debye spectral density, with $\lambda_{el} = 35\ cm^{-1}$, $\lambda_{vib} = 5\ cm^{-1}$ and $\omega_c = 53.3\ cm^{-1}$, for both electronic and vibrational degrees of freedom. The eigenstates formed by diagonalizing $H_{sys.ex}$ are shown in Figure 6. The table below shows the vibrational transition dipole moments (tdm) for the eigenstates, we enumerate only the ones that have sizable values.

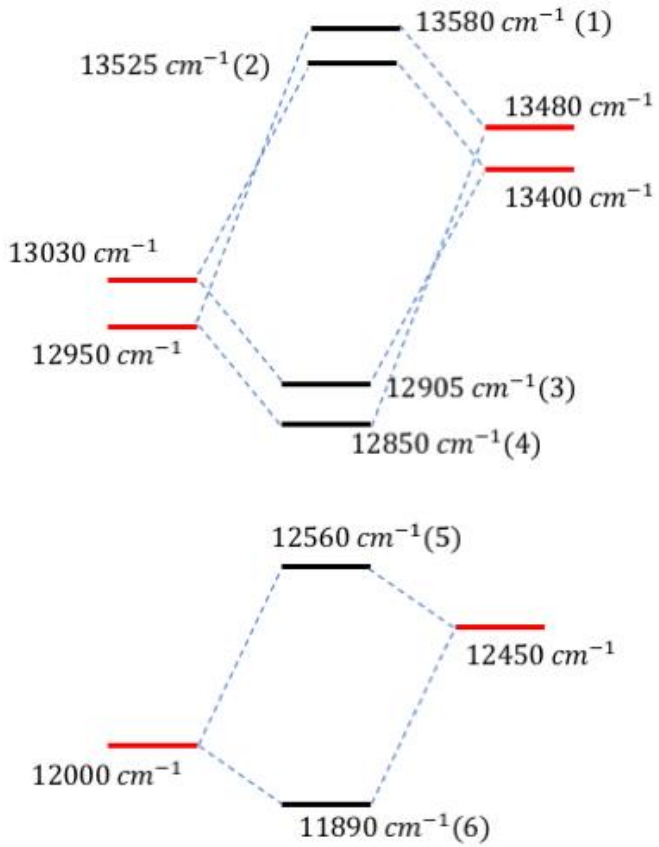

Figure 6. Site states (red) and vibronic level (black) along with their energies for the dimer model described in the text. The numbers in the text indicate the vibronic excitons from highest to lowest energy.

The total ESA rephasing signals at $t_2 = 0$ fs and $t_2 = 625$ fs are shown in Figures 7(a) and 7(b), respectively. Since each pathway can be computed separately, we are able to see that the signal arises mostly from the populations at excitons 5 $(12560\ cm^{-1})$ and 6 $(11890\ cm^{-1})$, the "electronic-only" eigenstates of $H_{sys.ex}$. Coherences do not contribute to the signal for these parameters.

Table II. Vibrational transition moments for the excited states of the dimer model

Tdm \ Vibrational	1	2	3	4	5	6
1					-1.0045	
2					-0.9903	
3						-0.9809
4						-1.0166
5	-1.0045	-0.9903				
6			-0.9809	-1.0166		

At long times, population relaxation becomes important. Therefore, at $t_2 = 625$ fs, the signal consists of populations that i) have started and stayed at the same exciton, Figure 7(c) shows these contributions from excitons 5 and 6, and ii) have relaxed from one exciton to another, downhill relaxation being more predominant. Figure 7(d) shows the relaxing population from 5 to 6. These contributions add up to give the total signal at $t_2 = 625$ fs in Figure 7(b).

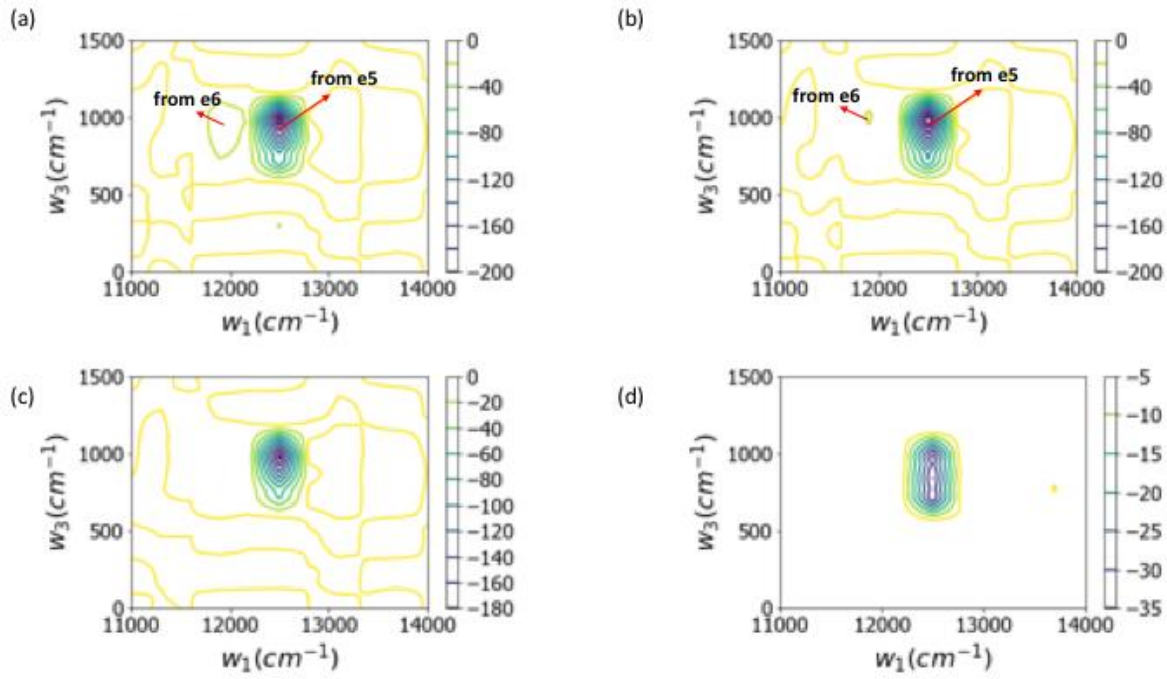

Figure 7. 2DEV spectra for ESA pathway for the model dimer system. (a) and (b) Total rephasing contribution at waiting times of 0 fs and 625 fs, respectively. (c) Population that has stayed at the initial excitons after 625 fs, and (d) relaxing population from exciton 5 to exciton 6 at 625 fs.

Also, unlike 2DES spectroscopy, the surviving (diagonal peaks in 2DES) and relaxing (off-diagonal peaks in 2DES) populations show up at roughly the same peak positions in 2DEV spectra. For instance, for exciton 5, the signal appears at $\{\varepsilon_5, (\varepsilon_1 - \varepsilon_5)\}$ and $\{\varepsilon_5, (\varepsilon_2 - \varepsilon_5)\}$ for surviving population and at $\{\varepsilon_5, (\varepsilon_4 - \varepsilon_6)\}$ and $\{\varepsilon_5, (\varepsilon_3 - \varepsilon_6)\}$ for relaxing population from 5 to 6. Here, $(\varepsilon_2 - \varepsilon_5)$ in the surviving pathway and $(\varepsilon_4 - \varepsilon_6)$ in the relaxing pathway have similar values. Also, $(\varepsilon_1 - \varepsilon_5)$ and $(\varepsilon_3 - \varepsilon_6)$ have similar values. For exciton 6, the signal appears at $\{\varepsilon_6, (\varepsilon_3 - \varepsilon_6)\}$ and $\{\varepsilon_6, (\varepsilon_4 - \varepsilon_6)\}$ for the surviving population.

Figure 8 shows the total rephasing signal, obtained by summing the contributions from the Ground State Bleaching (GSB) and Excited State Absorption (ESA) pathways, at (a) $t_2 = 0$ fs, and (b) $t_2 = 625$ fs. The positive signal stems from GSB pathway and the negative signal from the ESA pathway. Also, the signal is strongest at exciton 5, with faint contours at exciton 6.

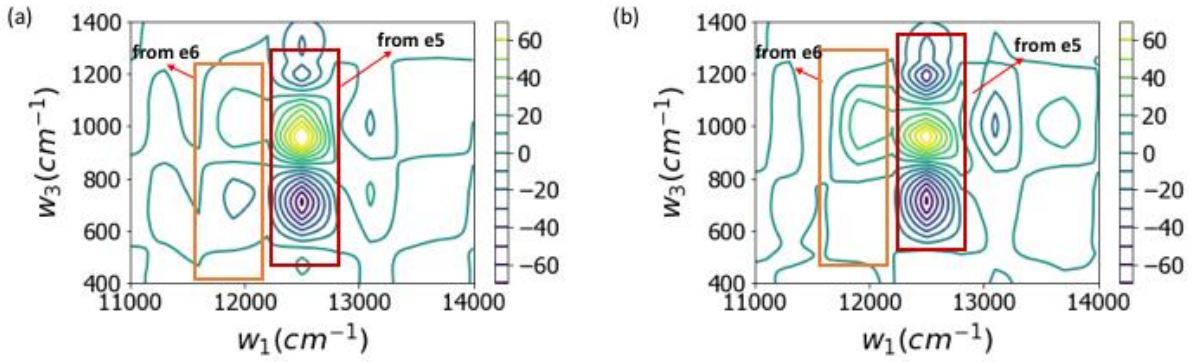

Figure 8. Total rephasing signal (GSB + ESA pathways) at (a) $t_2 = 0$ fs, (b) $t_2 = 625$ fs.

It is important to note that for the model dimer system with each monomer possessing a single vibration in both ground and excited electronic state, the six-exciton picture is accurate for all coupling strengths. However, for weakly coupled systems, specifically in the Forster limit, a number of vibrational transitions in the excited state become rigorously forbidden as they involve "cross molecule" transitions, for example, $\left|Y\ v_{g0}^{X} v_{e0'}^{Y}\right\rangle \rightarrow \left|Y\ v_{g1}^{X} v_{e0'}^{Y}\right\rangle$, where $\{X, Y\} \in \{A, B\}$. In this case the vibrational transitions observed in 2DEV spectra revert to the more intuitive flags indicating the location of electronic excitation.

Summary and Conclusions

2DEV spectroscopy, though still in its development stage, clearly demonstrates considerable promise for the study of complex molecular dynamics such as energy, electron, coupled proton-electron transfer, as well as molecular dynamics involving large structural changes.[27] The enhanced spectral resolution through the vibrational axis provides insights into electronic structural evolution, the spatial location of excitation in energy transfer complexes, and, through the information contained in the center line slope, provides a unique window into the correlation of electronic and vibrational evolution.[21] Further development of theory and modeling of the CLS dynamics is clearly needed to expose the full potential of this new quantity, but it has already proved very useful in describing conical intersection dynamics of triphenyl methane dyes.[27]

A key motivation for developing the technique was its expected sensitivity to vibronic coherences, which have recently been suggested to play a key role in primary photosynthetic charge separation in Photosystem II,[38–41] and in organic photovoltaic systems.[42–45] This required development of theoretical techniques to calculate 2DEV spectra for both strongly and weakly coupled systems. The application of our approach to weakly coupled (localized vibrations) is described above. Application to strongly coupled systems will be described in forthcoming publications.

Acknowledgements

This work was supported by the U.S. Department of Energy, Office of Science, Basic Energy Sciences, Chemical Sciences, Geosciences, and Biosciences Division under Field Work Proposal 449A. G. R. F. thanks Magdalen College, Oxford for a visiting Fellowship, and the Department of Physical and Theoretical Chemistry, Oxford for their hospitality during the writing of this paper. E.A.A. acknowledges the support of the Berkeley Fellowship

References

1 L. N. M. Duysens, *Prog. Biophys. Mol. Biol.*, 1964, **14**, 1–104.

2 G. W. Robinson, *Brookhaven Symp. Biol.*, 1966, **19**, 16–48.

3 H. Bergström, V. Sundström, R. van Grondelle, E. Åkesson and T. Gillbro, *Biochim. Biophys. Acta - Bioenerg.*, 1986, **852**, 279–287.

4 M. G. Müller, K. Griebenow and A. R. Holzwarth, *Biochim. Biophys. Acta - Bioenerg.*, 1991, **1098**, 1–12.

5 T. Joo, Y. Jia, J.-Y. Yu, D. M. Jonas and G. R. Fleming, *J. Phys. Chem.*, 1996, **100**, 2399–2409.

6 D. D. Eads, E. W. Castner, R. S. Alberte, L. Mets and G. R. Fleming, *J. Phys. Chem.*, 1989, **93**, 8271–8275.

7 H. Sumi, *J. Phys. Chem. B*, 1999, **103**, 252–260.

8 G. D. Scholes and G. R. Fleming, *J. Phys. Chem. B*, 2000, **104**, 1854–1868.

9 R. Agarwal, B. P. Krueger, G. D. Scholes, M. Yang, J. Yom, L. Mets and G. R.

Fleming, *J. Phys. Chem. B*, 2000, **104**, 2908–2918.

10 R. Agarwal, M. Yang, Q.-H. Xu and G. R. Fleming, *J. Phys. Chem. B*, 2001, **105**, 1887–1894.

11 M. Yang and G. R. Fleming, *Chem. Phys.*, 2002, **275**, 355–372.

12 T. Brixner, J. Stenger, H. M. Vaswani, M. Cho, R. E. Blankenship and G. R. Fleming, *Nature*, 2005, **434**, 625–628.

13 G. S. Engel, T. R. Calhoun, E. L. Read, T.-K. Ahn, T. Mančal, Y.-C. Cheng, R. E. Blankenship and G. R. Fleming, *Nature*, 2007, **446**, 782–786.

14 J. C. Dean, T. Mirkovic, Z. S. D. Toa, D. G. Oblinsky and G. D. Scholes, *Chem*, 2016, **1**, 858–872.

15 G. Panitchayangkoon, D. Hayes, K. A. Fransted, J. R. Caram, E. Harel, J. Wen, R. E. Blankenship and G. S. Engel, *Proc. Natl. Acad. Sci.*, 2010, **107**, 12766–12770.

16 A. Ishizaki and G. R. Fleming, *J. Chem. Phys.*, 2009, **130**, 234111.

17 V. Tiwari, W. K. Peters and D. M. Jonas, *Proc. Natl. Acad. Sci.*, 2013, **110**, 1203–1208.

18 Y. Fujihashi, G. R. Fleming and A. Ishizaki, *J. Chem. Phys.*, 2015, **142**, 212403.

19 T. A. A. Oliver, N. H. C. Lewis and G. R. Fleming, *Proc. Natl. Acad. Sci.*, 2014, **111**, 10061–10066.

20 J. K. Gillie, G. J. Small and J. H. Golbeck, *J. Phys. Chem.*, 1989, **93**, 1620–1627.

21 N. H. C. Lewis, H. Dong, T. A. A. Oliver and G. R. Fleming, *J. Chem. Phys.*, 2015, **142**, 174202.

22 N. H. C. Lewis and G. R. Fleming, *J. Phys. Chem. Lett.*, 2016, **7**, 831–837.

23 N. H. C. Lewis, N. L. Gruenke, T. A. A. Oliver, M. Ballottari, R. Bassi and G. R. Fleming, *J. Phys. Chem. Lett.*, 2016, **7**, 4197–4206.

24 V. Novoderezhkin, A. Marin and R. van Grondelle, *Phys. Chem. Chem. Phys.*, 2011, **13**, 17093.

25 G. S. Schlau-Cohen, T. R. Calhoun, N. S. Ginsberg, E. L. Read, M. Ballottari, R. Bassi, R. van Grondelle and G. R. Fleming, *J. Phys. Chem. B*, 2009, **113**, 15352–15363.

26 Z. Liu, H. Yan, K. Wang, T. Kuang, J. Zhang, L. Gui, X. An and W. Chang, *Nature*, 2004, **428**, 287–292.

27 E. C.-K. Wu, Q. Ge, E. A. Arsenault, N. H. C. Lewis, N. L. Gruenke, M. J. Head-Gordon and G. R. Fleming, *Phys. Chem. Chem. Phys.*, , DOI:10.1039/C8CP05264F.

28 T. Mančal, A. V. Pisliakov and G. R. Fleming, *J. Chem. Phys.*, 2006, **124**, 234504.

29 A. V. Pisliakov, T. Mančal and G. R. Fleming, *J. Chem. Phys.*, 2006, **124**, 234505.

30 B. J. Ka and E. Geva, *J. Chem. Phys.*, 2006, **125**, 214501.

31 L. Seidner, G. Stock and W. Domcke, *J. Chem. Phys.*, 1995, **103**, 3998–4011.

32 M. Cho, *J. Chem. Phys.*, 2001, **115**, 4424–4437.

33 L. Chen, R. Zheng, Y. Jing and Q. Shi, *J. Chem. Phys.*, 2011, **134**, 194508.

34 M. Baer, *Beyond Born-Oppenheimer*, John Wiley & Sons, Inc., Hoboken, NJ, USA, 2006.

35 P. Bhattacharyya and K. L. Sebastian, *Phys. Rev. E*, 2013, **87**, 062712.

36 P. Bhattacharyya and K. L. Sebastian, *J. Phys. Chem. A*, 2013, **117**, 8806–8813.

37 P. Bhattacharyya and N. Ananth, *arXiv:*1705.00738.

38 E. Romero, R. Augulis, V. I. Novoderezhkin, M. Ferretti, J. Thieme, D. Zigmantas and R. van Grondelle, *Nat. Phys.*, 2014, **10**, 676–682.

39 V. I. Novoderezhkin, E. Romero, J. Prior and R. van Grondelle, *Phys. Chem. Chem. Phys.*, 2017, **19**, 5195–5208.

40 F. D. Fuller, J. Pan, A. Gelzinis, V. Butkus, S. S. Senlik, D. E. Wilcox, C. F. Yocum, L. Valkunas, D. Abramavicius and J. P. Ogilvie, *Nat. Chem.*, 2014, **6**, 706–711.

41 G. D. Scholes, G. R. Fleming, L. X. Chen, A. Aspuru-Guzik, A. Buchleitner, D. F. Coker, G. S. Engel, R. van Grondelle, A. Ishizaki, D. M. Jonas, J. S. Lundeen, J. K. McCusker, S. Mukamel, J. P. Ogilvie, A. Olaya-Castro, M. A. Ratner, F. C. Spano, K. B. Whaley and X. Zhu, *Nature*, 2017, **543**, 647–656.

42 A. De Sio and C. Lienau, *Phys. Chem. Chem. Phys.*, 2017, **19**, 18813–18830.

43 S. M. Falke, C. A. Rozzi, D. Brida, M. Maiuri, M. Amato, E. Sommer, A. De Sio, A. Rubio, G. Cerullo, E. Molinari and C. Lienau, *Science (80-.).*, 2014, **344**, 1001–1005.

44 Y. Song, S. N. Clafton, R. D. Pensack, T. W. Kee and G. D. Scholes, *Nat. Commun.*, 2014, **5**, 4933.

45 Y. Song, C. Hellmann, N. Stingelin and G. D. Scholes, *J. Chem. Phys.*, 2015, **142**, 212410.